Ni-functionalized Ca@Si yolk-shell nanoreactors for enhanced integrated CO_2 capture and dry reforming of methane via confined catalysis

Shuzhuang Sun [a,b,c], Yuanyuan Wang [b], Yikai Xu [b,d], Hongman Sun [e], Xiaotong Zhao [b], Yingrui Zhang [b], Xiaoxiao Yang [c], Xuan Bie [c], Mengna Wu [c], Chen Zhang [b,f], Yuan Zhu [b], Yongqing Xu [c,*], Hui Zhou [c,g,**], Chunfei Wu [b,*]

[a] School of Chemical Engineering, Zhengzhou University, Zhengzhou 450001, China
[b] School of Chemistry and Chemical Engineering, Queen's University Belfast, Belfast BT7 1NN, UK
[c] Key Laboratory for Thermal Science and Power Engineering of Ministry of Education, Beijing Key Laboratory of CO2 Utilization and Reduction Technology, Department of Energy and Power Engineering, Tsinghua University, Beijing 100084, China
[d] Key Laboratory for Advanced Materials and Feringa Nobel Prize Scientist Joint Research Center, Frontiers Science Center for Materiobiology and Dynamic Chemistry, School of Chemistry and Molecular Engineering, East China University of Science and Technology, 130 Meilong Road, Shanghai 200237, China
[e] State Key Laboratory of Heavy Oil Processing, College of Chemistry and Chemical Engineering, China University of Petroleum, Qingdao 266580, China
[f] SINOPEC Economics & Development Research Institue Company Limited, Beijing 100029, China
[g] Shanxi Research Institute for Clean Energy, Tsinghua University, Taiyuan, Shanxi 030000, China

ARTICLE INFO

ABSTRACT

The emerging integrated CO_2 capture and utilization (ICCU) potentially contributes to net zero emissions with low cost and high efficiency. The catalytic performance in ICCU process is highly restricted by the equilibriums of carbonate decomposition and dry reforming of methane (DRM). Here, we engineer a unique yolk-shell dual functional nanoreactor construction to improve the catalytic performance via confined catalysis. By tailoring the carbonates decomposition kinetics and confining the CO_2 diffusion path, ~92% CO_2 conversion is achieved over (Ni/Ca)@Si and shows no distinct activity loss in 10 cycles at 650 °C. The formed Ca_2SiO_4 shells restrain the sintering of CaO yolks by acting as physical barriers, and stabilize the Ni particle size. It is also confirmed on in situ DRIFTS that the integrated DRM might occur via carbonyls, formates and CHO intermediates, in which formates species are highly dependent on Ni-carbonates interfaces.

1. Introduction

Carbon capture and utilization (CCU) technologies play pivotal roles in achieving net zero by this mid-century to relieve the climate and environmental issues caused by the greenhouse effect[1,2]. Specifically, CCU includes carbon capture (e.g., amine scrubbing[3,4] and calcium looping[5–8]) from point sources (e.g., power plants and cement factories)[9], CO_2 compression and transportation, and catalytic conversion (e.g., CO_2 methanation[10,11] and dry reforming of methane[12,13]) processes. Massive energy was consumed on temperature and pressure swing operations, severely restraining the wide deployment of such technologies[14]. Recently, an emerging integrated CO_2 capture and utilization (ICCU) technology has gained increasing interest from

researchers and engineers due to the outperformed low-cost and high efficiency[15–18]. Briefly, ICCU achieved direct conversion of captured CO_2 by gas swing between CO_2-containing exhaust gas (e.g., flue gas) and reducing agents (e.g., H_2[19,20] and CH_4[21,22]), in which the temperature-swing during adsorbents regeneration, CO_2 transportation, and CO_2 pre-heating before catalytic conversion processes are eliminated.

$$CH_4 + CO_2 = 2CO + 2H_2 \tag{1}$$

Among the CO_2 conversion reactions, dry reforming of methane (DRM, Eq.1) utilizing two green-house gases to yield syngas (CO+H_2), which could be further upgraded into valuable olefins and liquid chemicals via Fischer-Tropsch synthesis. Integrate CO_2 capture and

---

* Corresponding authors.
** Corresponding author at: Key Laboratory for Thermal Science and Power Engineering of Ministry of Education, Beijing Key Laboratory of CO2 Utilization and Reduction Technology, Department of Energy and Power Engineering, Tsinghua University, Beijing 100084, China.
E-mail addresses: xuyongqing@hust.edu.cn (Y. Xu), huizhou@tsinghua.edu.cn (H. Zhou), c.wu@qub.ac.uk (C. Wu).
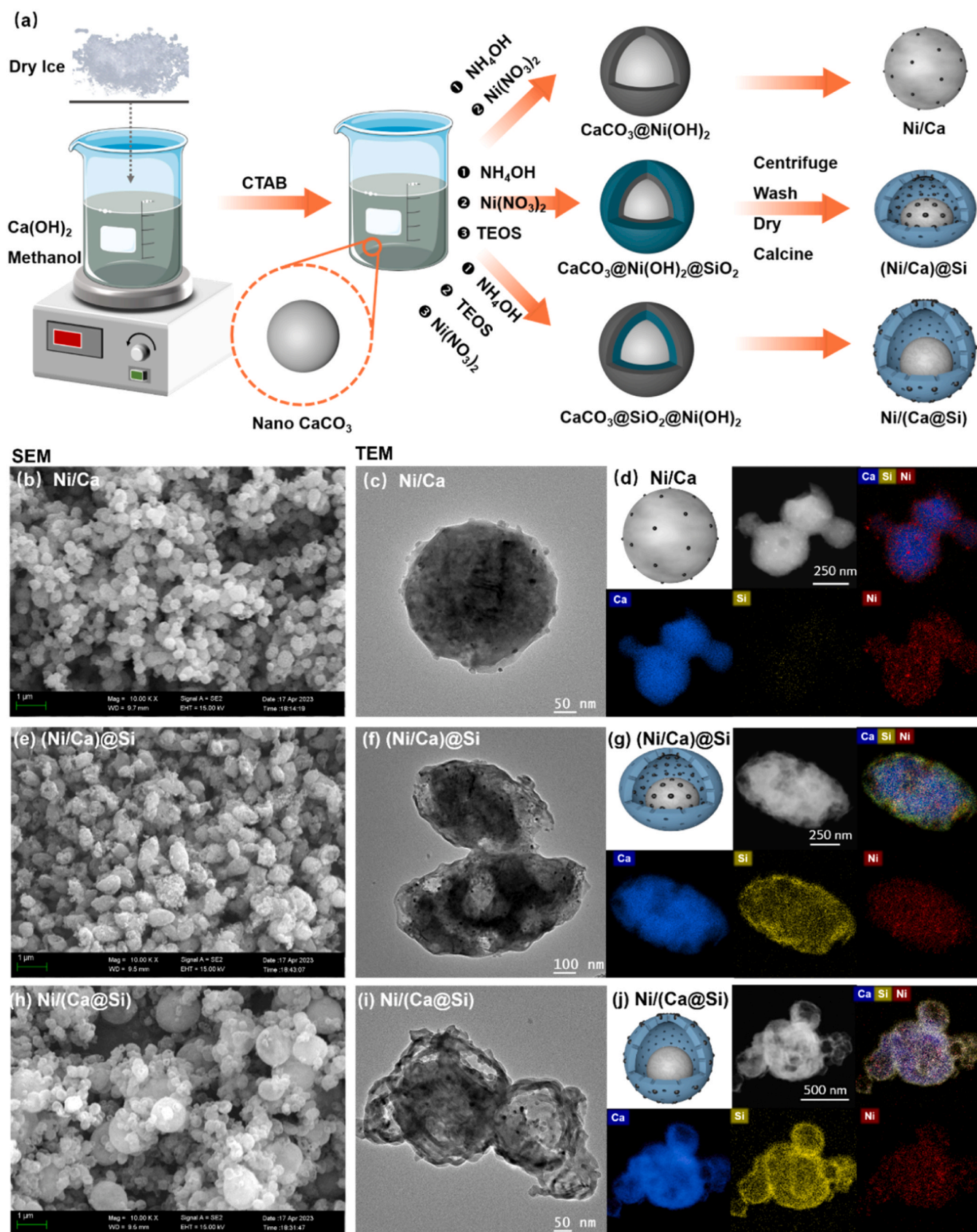
Fig. 1. Schematic diagram of the synthesis procedure of Ni/Ca and Ni functionalized Ca@Si yolk-shell nanoreactors (a); SEM and TEM-EDX-mapping images of reduced Ni/Ca (b, c and d), (Ni/Ca)@Si (e, f and g) and Ni/(Ca@Si) (h, i and j) materials.

DRM (ICCU-DRM) potentially contribute to a low-cost or profitable path for industrial CO_2 reduction[23–25]. Dual functional materials, consisting of CO_2 adsorbents and catalysts, are the keys to achieving CO_2 capture and in-situ conversion. To eliminate extra energy costs derived from temperature swings in ICCU, adsorbents and catalysts should work well under the same conditions. CaO and Ni have proven satisfactory partners for high-temperature CO_2 capture and catalytic conversion in ICCU-DRM[26,27]. However, the integrated DRM meets even more severe carbon deposition issues[24] compared to conventional DRM due to the much higher CH_4 partial pressure[28]. Furthermore, the CaO-based adsorbents exhibit significant volume swing and severe sintering during cyclic calcium looping in ICCU, which on the other hand aggravates the aggregation of loaded Ni by passive migration[21].

Abundant studies have focused on introducing thermally stable materials (e.g., ZrO_2[22] and Al_2O_3[29]) into Ni-CaO system to restraint CaO sintering for stable CO_2 capture cyclabilities, but little attention was paid on tailoring catalytic performance in the integrated DRM process. Notably, one of the reactants, CO_2, participates in DRM in ICCU via the form of carbonates, which is different from the conventional DRM process. The CO_2 exhibits a directional path (from carbonates to gas phase) in ICCU, and the decomposed CO_2 may bypass the catalytic sites and miss DRM catalytic reaction. It is hence a promising strategy to improve catalytic performance by constructing the spatial structure of the catalysts and adsorbents to effectively promote the contact probability between CO_2 and the catalyst. Confined catalysis was proposed to effectively promote the target reaction by confining reactants in an internal space[30,31] and alleviate deactivation by stabilizing the catalyst's structure[32]. The specific strategy is to build the catalytic active shell outside the carbonate core, and the decomposed CO_2 hence has to pass through the catalysts before it can be released into the gas flow. Controlled hydrolysis of silicone has reported mature strategy and makes it easy to construct porous structures[30,31]. Hence, Si was chosen as the shell material.

Furthermore, as a recently emerging process, the mechanism investigation of ICCU-DRM is far from convincing. Shao et al.[75] proposed the *H intermediate derived from CH_4 dehydrogenation on Ni overflow to nearby CaO surface and converted the $*CO_2$, while the *OH species generated from $*CO_2$ reduction participate in $*CH_2$ oxidation to form CO. Hu et al.[22] suggested that the formate species formed from adsorbed H species and CO_3^{2-} are responsible for CO formation in integrated DRM. The catalytic roles of Ni-carbonate interfaces in ICCU are also under debate[33,34]. There is a lack of a platform to systematically illustrate the independent roles of the above active candidates.

Herein, we construct Ca@Si yolk-shell adsorbents and anchor Ni in/ on the shell to obtain nanoreactors. Subsequently, we demonstrate the promotion effect of CO_2 capture kinetics and stabilities and the integrated DRM catalytic performance via confined catalysis. The hypotaxis of CH_4 decomposition and integrated DRM and side reaction inhibition strategy are discussed. Furthermore, we present a convincing mechanism verification platform with various active site candidates and illustrate their independent potential routes in the integrated DRM. Both the confined catalysis-directed yolk-shell dual functional nanoreactor construction strategy and reaction pathways investigation would provide valuable guidelines to further promote ICCU-DRM performance and other heterogeneous catalytic processes.

2. Methods

2.1. Preparation of nano-$CaCO_3$ suspension

The nano-$CaCO_3$ was synthesized by dry-ice precipitation method followed previously reported work[35], as illustrated in Fig. 1a. Specifically, 1.48 g (0.02 mol) $Ca(OH)_2$ (Sigma-Aldrich, $\geq$ 95%) was dispersed in 200 mL methanol (Sigma-Aldrich, $\geq$ 99.5%) with stirring. Dry ice was added to the solution and the temperature was kept at ~−50 °C for 3 h. Subsequently, 30 mL cetyltrimethylammonium bromide

(CTAB, Sigma-Aldrich, $\geq$ 99%) solution (0.364 g in 30 mL distilled water) was added to the suspension with stirring for 10 min to avert particle aggregation. The nano-$CaCO_3$ was dispersed and stabilized in methanol, named as nano-$CaCO_3$ suspension.

2.2. Preparation of Ni/Ca, (Ni/Ca)@Si and Ni/(Ca@Si) yolk-shell dual functional nanoreactors

A certain amount (1 mL) of NH_4OH (Sigma-Aldrich, 28% NH_3 in H_2O) was added into the nano-$CaCO_3$ suspension with 10 min stirring to facilitate the hydrolysis of TEOS and precipitate nickel. Subsequently, 0.29 g $Ni(NO_3)_2 \cdot 6 H_2O$ (Sigma-Aldrich, $\geq$ 98.5%) were dissolved in 10 mL methanol and then dropped into the nano-$CaCO_3$ suspension and stirred for 30 min. The suspension was centrifuged and washed with methanol three times and then dried at 70 °C for 2 h under vacuum. Finally, the sample was calcined at 800 °C for 1 h with a heating rate of 2 °C/min to obtain Ni/Ca.

The (Ni/Ca)@Si and Ni/(Ca@Si) yolk-shell dual functional nanoreactors were synthesized by introducing an extra silica coating process (Fig. 1a). Briefly, 1 mL NH_4OH (a.q.) was dropped into the nano-$CaCO_3$ suspension with 10 min stirring. Then, 0.29 g $Ni(NO_3)_2 \cdot 6 H_2O$ (dissolved in 10 mL methanol) was added into the nano-$CaCO_3$ suspension and stirred for 10 mins, followed by dropping 10 mL 10 mol% tetraethyl orthosilicate (TEOS, Sigma-Aldrich, $\geq$ 98%) into methanol solution with 3 h stirring. The suspension was then washed, centrifuged, dried and calcined as abovementioned processes to obtain calcined (Ni/Ca)@Si. The calcined Ni/(Ca@Si) was prepared by swapping the adding order of $Ni(NO_3)_2 \cdot 6 H_2O$ and TEOS. Before the evaluation, the NiSiCa-based materials were reduced at 700 °C for 1 h in 5% H_2/Ar to obtain reduced materials.

2.3. Materials characterizations

Inductively coupled plasma-optical emission spectrometry (ICP-OES): The materials were digested in nitric acid under microwave and the Ni, Si and Ca contents were analyzed by ICP-OES (Agilent ICPOES730).

N_2 physisorption: The porosities of materials were characterized by isothermal N_2 adsorption-desorption at 77 K on Autosorb iQ Station. And the micro and meso pore size distributions were analyzed by Horváth-Kawazoe (HK) and Barrett-Joyner-Halenda (BJH) methods using the desorption branch, respectively.

Electron microscopy: The surface morphologies of the synthesized nanoreactors were monitored on a scanning electron microscope (ZEISS Merlin® FE-SEM). The detailed morphologies and element distribution were characterized by transmission electron microscope on JEOL JEM-2010 with energy dispersive spectroscopy (EDS). The Ni particle size distributions were measured and plotted by Nano Measurer 1.2. The average particle diameter (d_{ave}) was calculated based on Eq.2.

$$d_{ave} = \frac{\sum(n_i d_i^3)}{\sum(n_i d_i^2)} \tag{2}$$

X-ray diffraction (XRD): The phase composition was characterized by XRD using a PANalytical Empyrean X-ray Powder Diffractometer (45 kV and 40 mA), equipped with a Cu Kα x-ray source. The data was collected in the 10–90° 2 Theta range and analyzed on MDI Jade 6.0.

Temperature-programmed CO_2 adsorption-desorption: The isothermal and programmed thermogravimetric analysis (TGA) were collected on a Hi-Res TGA 2950 thermogravimetric analyzer. Specifically, the temperature-programmed CO_2 adsorption-desorption analysis was carried out in 100 mL/min 15% CO_2/N_2 from 100 to 850 °C with a heating rate of 10 °C/min. The isothermal TG experiment was performed at 650 °C in 100 mL/min 15% CO_2/N_2 for 25 min, followed by 100 mL/min N_2 (BOC.co, 99.9%) for 45 min. To exclude the change of CaO-based materials under atmosphere storage (steam or CO_2

adsorption), all the materials were in situ pre-calcined in N_2 at 800 °C for 30 min.

X-ray photoelectron spectroscopy (XPS): The surface/interface element compositions and states of the synthesized nanoreactors were determined by XPS on Thermo Fisher ESCALAB 250Xi with Mg Kα X-ray source.

Raman spectroscopy: The deposited carbon species were presented by Raman spectroscopy on the WITec Alpha 300 R Confocal Raman Microscope equipped with a 532 nm diode laser (10 mW). The spectrums of each material was generated from three different sample areas.

2.4. ICCU-DRM evaluation

The ICCU-DRM reactions with nanoreactors were evaluated in a fixed-bed quartz wall reactor (Figure S1, OD: 12 mm; ID: 10 mm; L: 600 mm). 0.5 g material was fixed in the middle of the reactor by quartz wool and heated by a tubular furnace (Elite TSH 12/50/300–2416CG). Moreover, the thermocouple was placed in the middle of the reactor to control the temperature.

The ICCU-DRM experiment was performed by gas swing among 15% CO_2 (CO_2 capture step), N_2 (purge step) and 10% CH_4 (DRM step). Specifically, the material was heated to 700 °C and in situ reduced under 100 mL/min 5% H_2/Ar for 1 h (pre-processing). The ICCU mainly includes two steps for CO_2 capture and in situ DRM. In the first step, 100 mL/min 15% CO_2/N_2 was introduced for 20 min, followed by N_2 purge for 3 min. In the second step, 10% CH_4/N_2 was switched into the reactor until no more CO was generated. The cyclic ICCU-DRM evaluations were exhibited by repeating the above steps with an extra 5 mins' N_2 purge among each cycle. The outlet gas was monitored by an online gas analyzer (Enerac 700 AV) equipped with a Non-Dispersive InfraRed (NDIR) detector and H_2 thermal conductivity detector (CIXI-CX-H02).

The quantitative analysis was calculated by integrating the signal of reactants and products in different step regions. Notably, the carbon deposition in the DRM step would retain to the following CO_2 capture step and then compete with CO_2 capture via the reverse Boudouard reaction (Eq.3). The CO_2 capture capacities (C_{CO2}) were hence calculated by subtracting half of CO production from CO_2 consumption in CO_2 capture step (Eq.4). (CO_2^b: benchmark signal)

$$CO_2 + C = 2CO \tag{3}$$

$$C_{CO2}(mmol/g) = \frac{\int (CO_2^b - CO_2 - 0.5 * CO)dt * 1.667mL/s}{22.4mmol/mL * 0.5g} \tag{4}$$

The CO (Y_{CO}) and H_2 (Y_{H2}) yields were integrated in the DRM step as follows:

$$Y_{CO}(mmol/g) = \frac{\int COdt * 1.667mL/s}{22.4mmol/mL * 0.5g} \tag{5}$$

$$Y_{H2}(mmol/g) = \frac{\int H_2 dt * 1.667mL/s}{22.4mmol/mL * 0.5g} \tag{6}$$

Due to the detection limitation on steam, the CO_2 conversion rate (X_{CO2}) was calculated based on CO_2 capacities and unreacted CO_2 (Y_{CO2}) in the DRM step, as listed below:

$$Y_{CO2}(mmol/g) = \frac{\int CO_2 dt * 1.667mL/s}{22.4mmol/mL * 0.5g} \tag{7}$$

$$X_{CO2}(\%) = \frac{C_{CO2} - Y_{CO2}}{C_{CO2}} * \% \tag{8}$$

The CO_2 removal efficiency represents the extent to which CO_2 is removed. It was calculated via below equation:

$$R_{CO2} = \frac{CO_2^{input} - CO_2^{output}}{CO_2^{input}} * 100\% \tag{9}$$

2.5. In situ diffused reflectance infrared fourier transform spectroscopy (DRIFTS)

The in situ DRIFTS was carried out on PerkinElmer Spectrum equipped with a Mercury Cadmium telluride (MCT) detector (4 cm^{-1} resolution, 1000–4000 cm^{-1} range). To identify the surface intermediates in the ICCU-DRM process, two sets of in situ DRIFTS experiments were exhibited: isothermal ICCU-DRM and temperature-programmed DRM.

2.5.1. Isothermal ICCU-DRM in situ DRIFTS
The materials were in situ reduced in the cell under 5% H_2/Ar at 700 °C for 30 min and then equilibrated to 650 °C in Ar for 10 min. The spectrum was collected as the benchmark and subtracted, and subsequently, the 15% CO_2/N_2 was introduced for 90 s as the CO_2 capture step. And then switch into N_2 for 300 s to purge the residual CO_2 and unstable surface species, followed by introducing 10% CH_4/N_2 for 500 s in the DRM step. The spectra were collected every 10 s from inletting CO_2 to exhibit the surface species changes under ICCU-DRM conditions.

2.5.2. Temperature-programmed DRM in situ DRIFTS
The integrated DRM was investigated under temperature-programmed conditions (100–750 °C). The materials were in situ reduced as above, followed by carbonating at 650 °C for 30 min under 15% CO_2/N_2. The cell was cooled down to 100 °C in 15% CO_2/N_2 and then purged for 10 min under N_2 for benchmark subtraction. Subsequently, 10% CH_4/N_2 was introduced with a heating rate of 50 °C/3 min up to 750 °C.

3. Results and discussion

3.1. The construction of Ni-functionalized Ca@Si yolk-shell nanoreactors

The $CaCO_3$ easily re-crystallizes in synthesis and yields large and anisotropic crystals[36], challenging the coating process in core-shell structure construction. In order to synthesize $CaCO_3$ with uniformly spherical morphology, introducing continuous disturbance[37] during the carbonates precipitation process to build miscellaneous crystals and lowering the temperature[38] to suppress recrystallization are considered to be effective strategies. Herein, dry ice was applied as the CO_2 source and provided satisfactory disturbance in the sublimation process in carbonate synthesis (Fig. 1a). As shown in Fig. 1b and c, the abovementioned synthesis strategy successfully directs the construction of spherical particles, and the Ni could be uniformly deposited in such a one-pot synthesis procedure. Further construction of core-shell nanoreactors inspired by confined catalysis requires the hydrolysis of silane on the surface of calcium carbonate (Fig. 1a). CTAB was introduced after carbonate precipitation to stabilize suspension[39] and subsequently acted as the template in silica deposition[40]. As shown in Fig. 1e-j, although silane would inevitably form micelles spontaneously to form SiO_2 cavities, the silica coating on calcium was well constructed. Furthermore, the volume shrinkage of calcium carbonate decomposition [41] and the formation of Ca_2SiO_4 shell during calcination in situ induced the formation of yolk-shell structures.

Notably, the various coating sequences of nickel and silica derived different nanoreactor morphologies. Loading silica after nickel induces spindle-shaped nanoreactors (Fig. 1e and f), while reverse deposition order constructs spherical structures with larger cavities (Fig. 1h and i). The induction mechanism is unclear, which might be attributed to the carbonate surface modification by nickel deposition or the interaction of calcium and silica in the calcination process. However, in any case, the successful encapsulation of calcium by silicon provides a convincing platform for subsequent performance and mechanism investigation. And the presented synthesis approach allows a wide modification for producing materials with various characteristics, such as adjusting silane

Table 1
Elemental analysis and porosity characterizations of NiSiCa-based materials.

Materials	ICP (wt%)			S_{BET} (m²/g)	V_{micro} (m³/g)	V_{meso} (m³/g)
	Ni	Si	Ca			
Ni/Ca	2.78	——	34.13	12.56	0.0031	0.088
(Ni/Ca)@Si	2.26	4.47	38.00	28.72	0.0097	0.35
Ni/(Ca@Si)	2.28	3.47	31.01	23.57	0.0082	0.13

amount for different shell thickness.

3.2. Characterizations of Ni-functionalized Ca@Si yolk-shell nanoreactors

Apart from the morphology analysis, more detailed characterizations were carried out to fully describe the synthesized nanoreactors. As evidenced by ICP results in Table 1, the three materials were synthesized with identical Ni loadings to exclude the performance differences caused by various active phase content. The Si and Ca fractions were also well controlled over two different nanoreactors. XPS was applied to evaluate the surface element fraction ($\sim$ 1–10 nm depth) [42], as detailed in Figure S2 and Table S1. The silica of (Ni/Ca)@Si and Ni/(Ca@Si) concentrated on the surface, as observed from the TEM results (Fig. 1g and j). Notably, the Ni contents on these two nanoreactors were similar (1–1.1 at%, Table S1), indicating the Ni distributed closely to the thin shell (Figs. 1f and i).

The phase fractions of various materials were analyzed by XRD, as shown in Figs. 2a and b. After calcination of as-synthesized materials, most of the carbonates decomposed and part of CaO reacted with SiO₂ to form the Ca₂SiO₄ phase. Notably, as evidenced in the internal pattern in Fig. 2b, the Ni/(Ca@Si) exhibited higher Ca₂SiO₄ crystallinity compared to (Ni/Ca)@Si. It is speculated that loaded Ni would physically obstruct the direct contact of calcium and silica, hence restricting the formation of huge Ca₂SiO₄ crystallite phase on (Ni/Ca)@Si. The binding energy shift in XPS also verified the formation of Ca₂SiO₄. The electron density and electronegativity of atoms exhibit various shielding effects of core electrons [43]. Introducing atoms with higher electronegativities (e.g. X_{Si}=1.7) would attract electrons from bulk atoms (e.g. X_{Ca}=1) and weaken the shielding effect on core electrons, hence increasing the binding energy of bulk elements. The Ca 2p XPS (Figure S2e) peaks of (Ni/Ca)@Si and Ni/(Ca@Si) shift to higher binding energy by $\sim$ 0.6 eV, indicating the extensive combination of silica and calcium (Si-O-Ca in the form of Ca₂SiO₄) on the surface. More clearly, the O1s (Figure S2f) of nanoreactors splits into two peaks at 530.5 and 531.5 eV, assigning to Ca-O-Ca and Ca-O-Si, respectively. The NiO was detected as the only Ni-containing crystal phase (Fig. 2a), consisting of Ni 2p characterization in XPS (Figure S2c, no distinct shift excluding the possibility of the widespread existence of Ni-O-Si).

The residual CaCO₃ on NiSiCa-based materials were thoroughly consumed in 5% H₂/Ar reduction at 700 °C, evidenced by the disappearance of CaCO₃ peaks in Fig. 2b. However, the NiO reduction is not obvious, which might be attributed to the encapsulated NiO species with poor H₂ accessibility. Furthermore, a small amount of Ca(OH)₂ was formed in the material due to air exposure during materials storage.

The coated silica acts as the shell of the nanoreactors, which needs to achieve both good confinement and mass transfer of reactants and products. The porosity of the shell is hence pivotal for such unique requirements. As listed in Table 1, the synthesized Ni/Ca as a benchmark exhibits poor porosity with 12.56 m²/g surface area, 0.0031 m³/g and 0.088 m³/g micro/mesopores volumes, respectively. The uniform CaO spheres exhibit $\sim$ 300 nm diameter, which could provide $\sim$5.97 m²/g
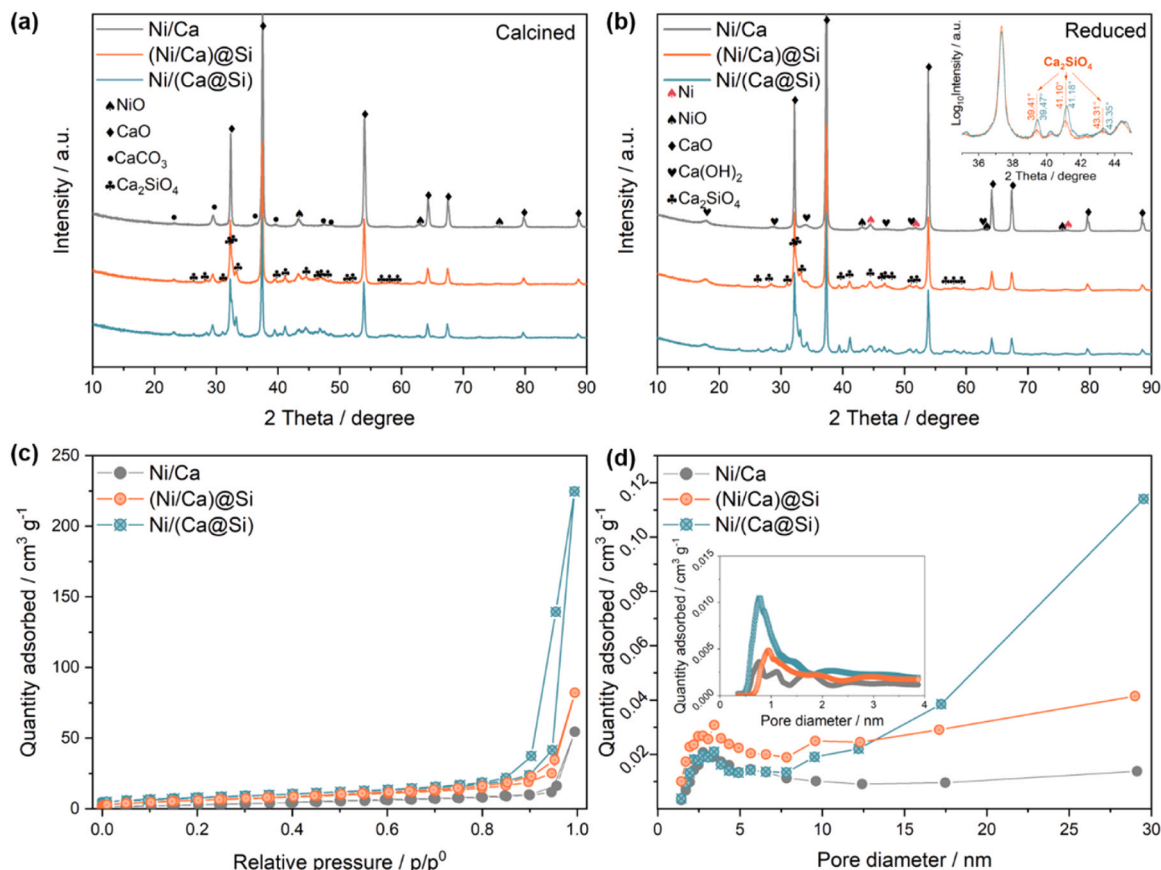

Fig. 2. The XRD patterns of calcined (a) and reduced (b) materials; The N₂ adsorption–desorption isotherms (c) and pore size distributions (d) of calcined materials.
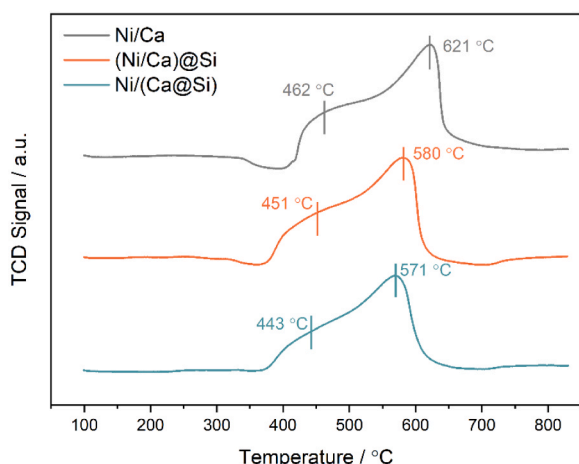
Fig. 3. TPR curves of calcined Ni/Ca, (Ni/Ca)@Si and Ni/(Ca@Si) materials.

surfaces (CaO density: 3.35 g/cm^3). Apparently, the tested surface area is higher than the theoretical value, which is explained by the defects and cracks observed in SEM images (Fig. 1b). As a comparison, the (Ni/Ca)@Si and Ni/(Ca@Si) nanoreactors perform doubled surface area and multiple micro/mesopores volumes, indicating the formation of porous shells. As shown in Figs. 2c and d, the nanoreactors exhibited distinct hysteresis loops in adsorption-desorption isotherms and enhanced micro/mesopores distributions. Specifically, the Ni/(Ca@Si) shows more pores with the diameter of 10–30 nm (Fig. 2c), which is highly attributed to the abundant cavities as discussed in Section 3.1.

The reducibility of metal oxides indicates the existing reducible species, which is an important indicator of metal-support interaction and metal distributions. As shown in Fig. 3, the H$_2$-TPR further confirms the existence of similar Ni species based on analogous H$_2$ consumption curves. Specifically, Ni/Ca exhibits two main reduction peaks at 462 and 621 °C, which are respectively attributed to the reduction of free and metal-support interacted NiO species[44,45]. It is controversial about the existing form of interacted NiO carried on irreducible supports. Some researchers suggest that the NiO reacts with MO$_x$ to form Ni$_x$M$_y$O$_z$ spinel to present strongly interacted NiO[46,47], while others deem that the interaction could be defined by encapsulation or even contact in the absence of spinel formation[48,49]. Based on the previous XRD and XPS analysis, the nickel presents in the NiO form on the synthesized nano-reactors and no Ni-containing spinel (i.e. NiAl$_2$O$_4$) formation was identified. It is hence reasonable to conclude that the NiO reduction peak at higher temperatures is contributed from the encapsulated NiO by CaO or Ca$_2$SiO$_4$. The metal particle size is widely believed inversely proportional to the reduction temperature[50,51]. However, as summarized in Figs. S3a-c, the average Ni particle sizes are positively related to the reduction temperature of both reduction peaks. It is inferred that the degree of encapsulation on NiO species might decrease from Ni/Ca to NiSiCa-based nanoreactors, indicating that the CaO exhibits more severe encapsulation effect on NiO.

3.3. ICCU-DRM performance

The ICCU has two steps: (i) CO$_2$ capture and (ii) in situ catalytic conversion. The temperature is highly sensitive for CO$_2$ capture using CaO-based adsorbents[52,53]. As shown in Fig. 4a and b, the materials performed differentiated carbonation kinetics. Ni/Ca started to capture CO$_2$ from ∼ 500 °C, while (Ni/Ca)@Si and Ni/(Ca@Si) nanoreactors could carbonate at even ∼ 400 °C. It was reported that smaller CaO particles had promoted carbonation kinetics at low temperatures due to
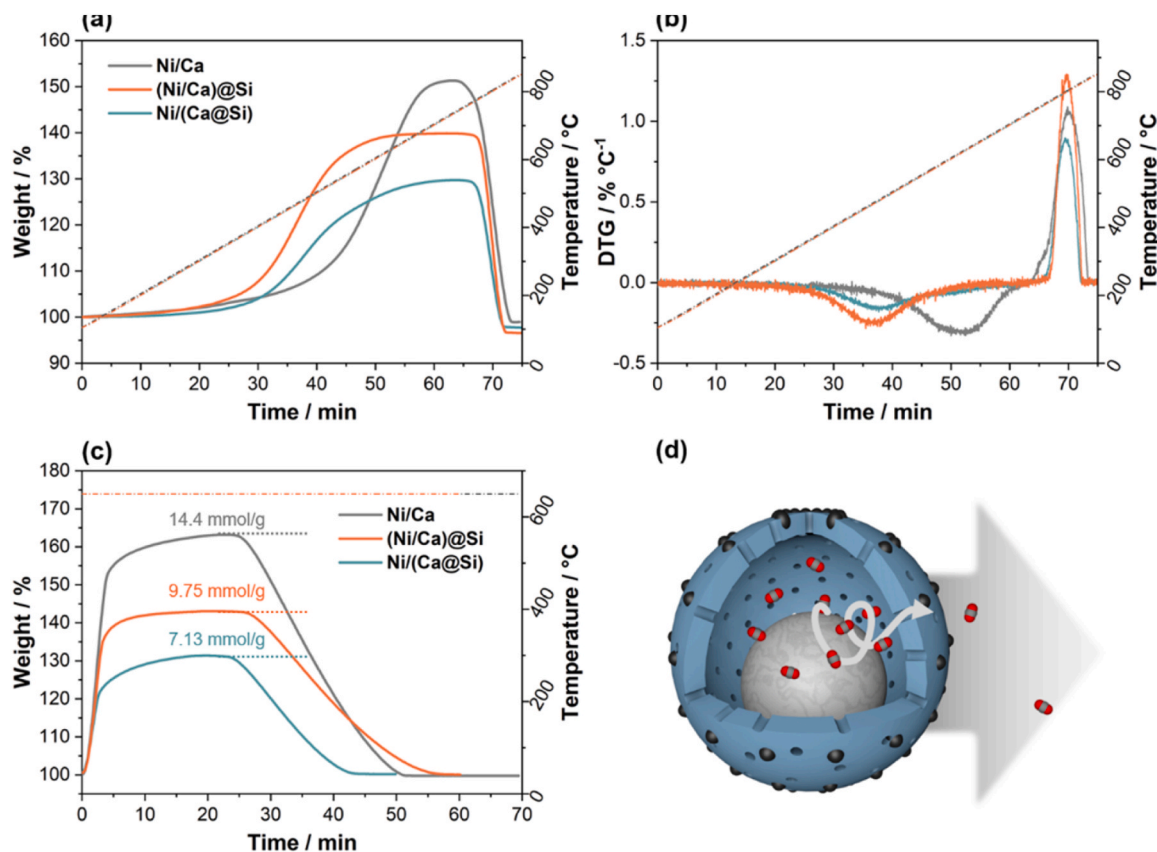

Fig. 4. The temperature programmed CO$_2$ adsorption-desorption curves of calcined materials: (a) TGA and (b) DTG; (c) The isothermal CO$_2$ adsorption-desorption curves of calcined materials; (d) The schematic diagram of CO$_2$ desorption on Ni/(Ca@Si) nanoreactor.
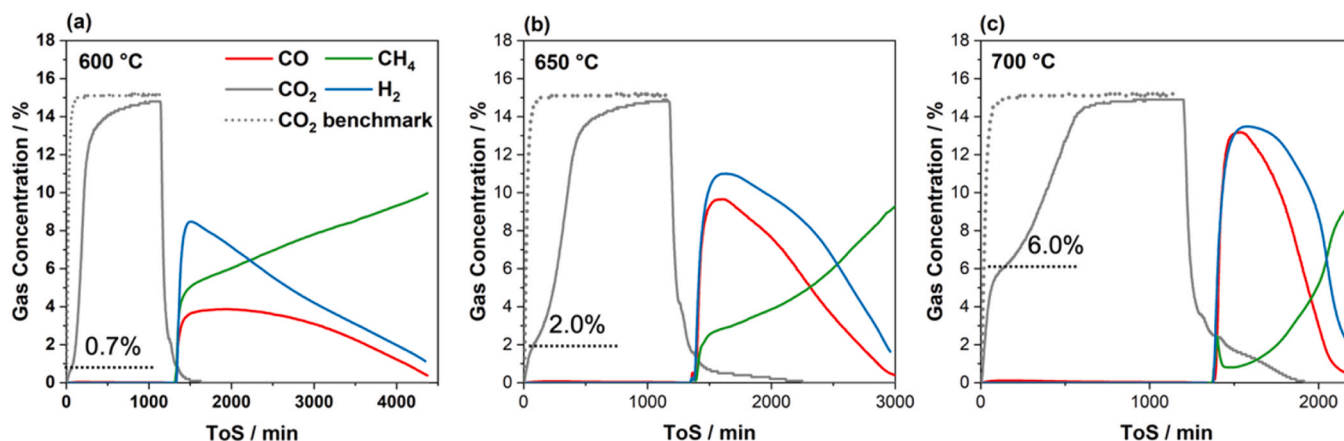
Fig. 5. Real time ICCU-DRM performances under various temperatures using Ni/(Ca@Si) nanoreactors: (a) 600 °C; (b) 650 °C and (c) 700 °C.

a more abundant surface and shorter diffusion distance[54]. As detailed in Fig. 1, the significantly smaller and looser CaO core after silica coating (Figs. 1f and i) fundamentally contributes to such enhancement in CO_2 capture. With the temperature increasing, the formed carbonates started to decompose quickly from ~750 °C, and all three candidates performed similarly. A proper temperature of ICCU should permit satisfactory carbon capture efficiency in the CO_2 capture step and appropriate decomposition kinetics in the integrated DRM step. Operating ICCU at a lower temperature would restrict the overall process efficiency, while applying too high temperature would excessively accelerate decomposition and limit the CO_2 conversion rate. As evidenced in Fig. 4, in which the carbonation kinetics reached the peak at ~500 °C and decomposition significantly occurred from ~700 °C, it is hence recommended that 500~700 °C is suitable for CO_2 capture using CaO-based materials.

Besides the enhanced CO_2 capture performance at lower temperatures, the (Ni/Ca)@Si and Ni/(Ca@Si) nanoreactors exhibited the expected decomposition results under 650 °C isothermal conditions. As shown in Fig. 4c, the Ni/Ca exhibited the highest CO_2 capacity (~
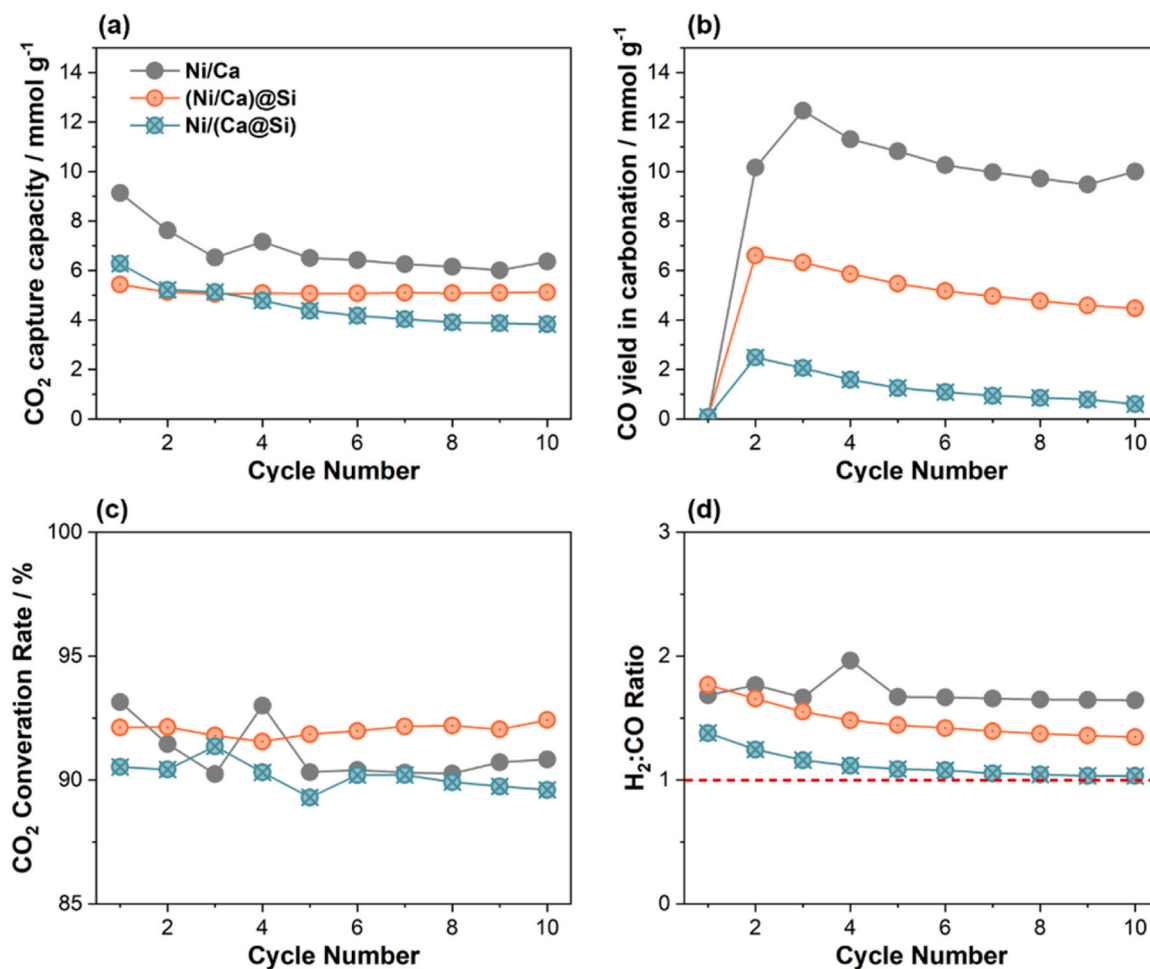

Fig. 6. Cyclic ICCU-DRM performances of the materials in 10 cycles: (a) CO_2 capture capacities and (b) CO yield in the CO_2 capture step; (c) CO_2 conversion and (d) H_2:CO ratio in the DRM step.
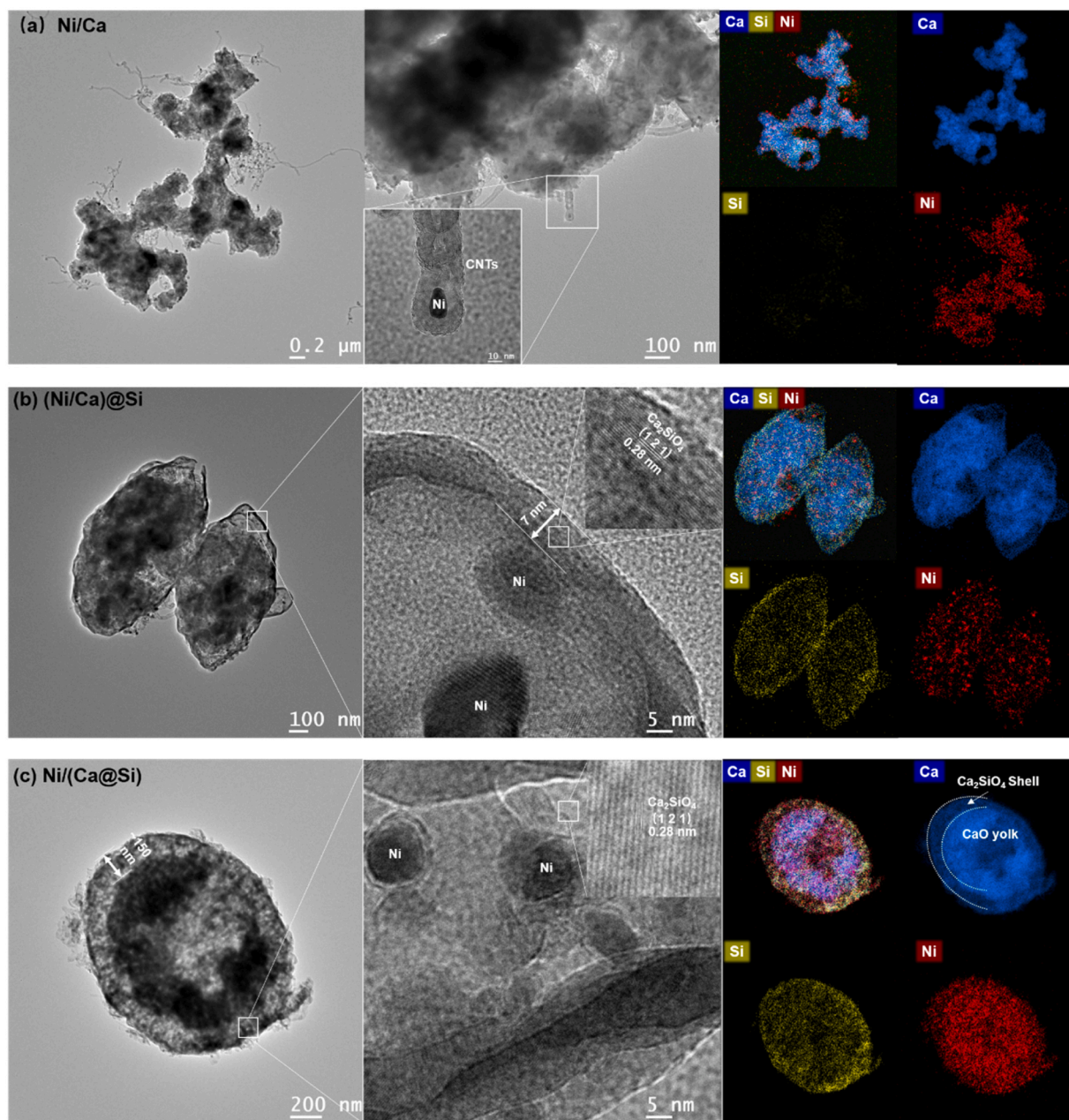
Fig. 7. TEM-EDX-mapping images of spent (a) Ni/Ca, (b) (Ni/Ca)@Si and (c) Ni/(Ca@Si) nanoreactors after 10 cycles.

14.4 mmol/g) due to the highest CaO molar fraction. Introducing silica would decrease CaO fraction and consume CaO by forming Ca_2SiO_4, hence showing lower CO_2 capacities ($\sim$ 9.75 and 7.13 mmol/g for (Ni/Ca)@Si and Ni/(Ca@Si), respectively). Notably, the carbonates decomposition of nanoreactors is slower than the Ni/Ca benchmark, which indicates the successful preparation of confined nanoreactors. As illustrated in Fig. 4d, the porous shell provided confined cavities and extended the residual time of CO_2 after decomposing from carbonates. Riveting the catalyst on the shell would reasonably increase the contact probability between CO_2 and the catalyst, promoting the catalytic performance.

The temperature effect is further evaluated under ICCU conditions to obtain the real-time CO_2 capture kinetics and the following DRM catalytic performance. The CO_2 removal efficiency represents the extent to which CO_2 is removed in the flue gas. As shown in Fig. 5, the initial CO_2 removal efficiency of Ni/(Ca@Si) decreases from $\sim$ 95% at 600 °C to $\sim$ 60% at 700 °C. The equilibrium of Eq.8 shifts to carbonate

decomposition under higher temperatures due to the endothermic properties of the decomposition process, which was also evidenced by the increased CO_2 release at higher temperatures in the DRM step. The DRM, as a strongly endothermic reaction, favors high temperatures[12]. Notably, the CO_2 is restricted by carbonate decomposition, hence interfering with the effect of temperature on the integrated DRM. However, although a low process temperature ensures better CO_2 removal in the CO_2 capture step, $\sim$ 3000 s is needed to thoroughly consume the carbonates in the DRM step. Overall, proper process temperature should fit satisfactory CO_2 capture performance and synergy carbonates decomposition and DRM kinetics. Considering the further deployment of ICCU, the residence time of CO_2 capture and DRM steps should be equal for continuous operation under mature dual fluid bed systems. Hence, 650 °C was selected as the optimal ICCU temperature with almost equal time periods of CO_2 capture and DRM.
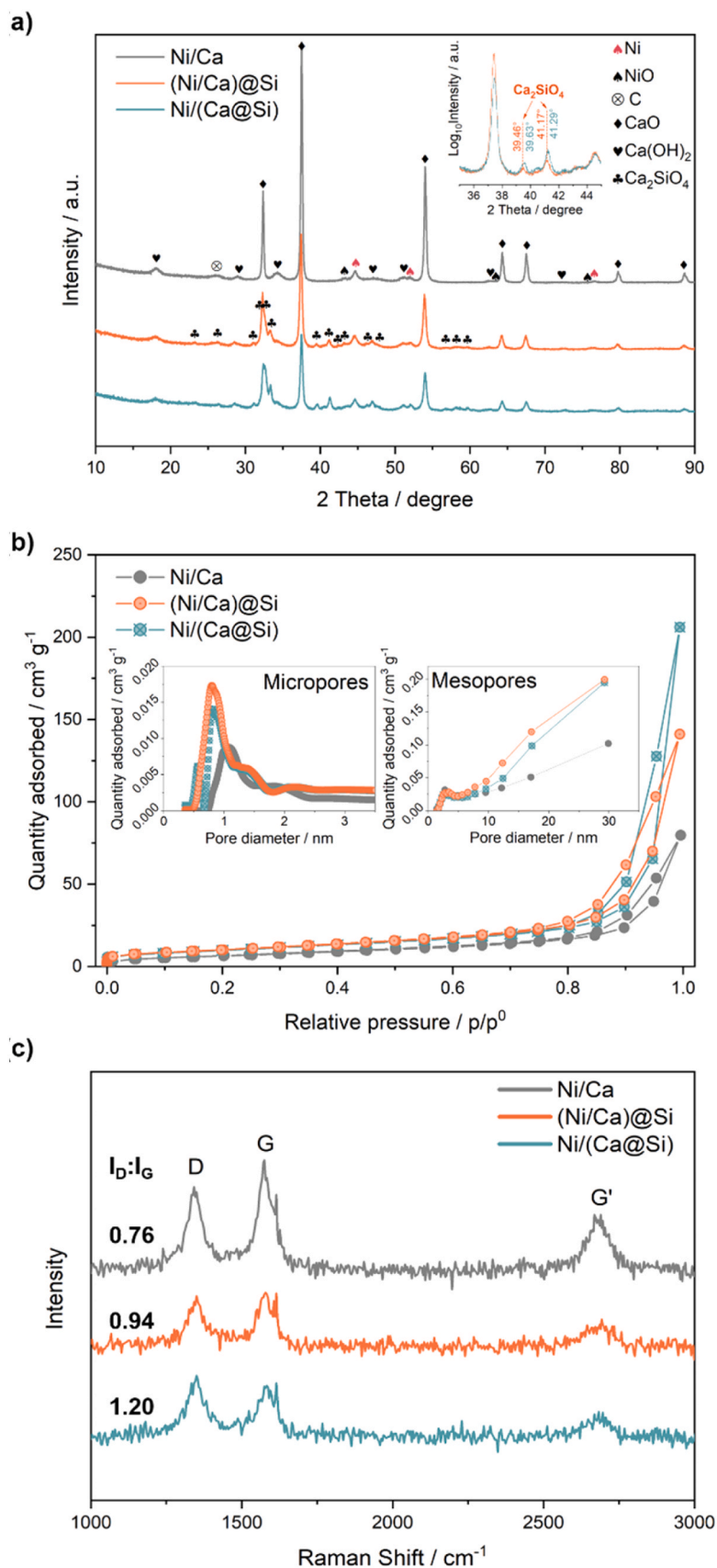
$$CaO + CO_2 \leftrightarrow CaCO_3 \tag{8}$$

a)

b)

c)
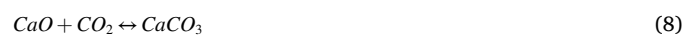
Fig. 8. (a) XRD patterns, (b) N_2 adsorption–desorption isotherms with micro-meso pore size distributions and (c) Raman spectrums of spent materials.

Ten cyclic ICCU evaluation was carried out to evaluate the stabilities of Ni/Ca, (Ni/Ca)@Si and Ni/(Ca@Si) (Fig. 6 and S4). As a benchmark, the CaO without Ni functionalization exhibits no activity in ICCU-DRM (Figure S5). In the integrated DRM process, the CH_4 decomposition inevitably occurs as a side reaction, and deposits carbon on the materials [21,24] (Fig. 7a as an example). The carbon would be then gasified by CO_2 in the carbon capture step (Figure S4) and obstruct the quantification of CO_2 capacities. Notably, the reverse Boudouard reaction might compete with carbonation in the initial time of CO_2 capture; however, 20 mins of carbonation is enough for saturating the adsorbents. The integrated CO_2 capacities in Fig. 6a were calculated by deducting half of CO production from CO_2 consumption, as detailed in Eq.4. The (Ni/Ca) @Si showed stable CO_2 uptake capacities, only decreasing from 5.43 to 5.12 mmol/g in cyclic evaluations (Fig. 6a), and the nanoparticles remain separated (Fig. 7b). The thickness of the Ca_2SiO_4 shell on (Ni/Ca) @Si was well maintained (Figs. 1g and 7b), implying the nickel intermediate layer does well in controlling the contact of calcium and silica. As a comparison, the Ni/Ca exhibited the highest initial CO_2 capacity due to the highest CaO fraction and gradually decreased from 9.13 to 6.36 mmol/g in 10 cycles due to sintering (significant particle aggregation in Fig. 7a). Similarly, the Ni/(Ca@Si) performed a capacity loss from 6.28 to 3.83 mmol/g. As shown in Fig. 7c, although the nanoparticles the Ca_2SiO_4 shell on Ni/(Ca@Si) significantly thickens to ∼ 150 nm, which might hinder CO_2 diffusion and capacities. The increase of the thickness might be attributed to the shell reconstruction in cyclic evaluation, especially the merge of small Ca_2SiO_4 species (Fig. 1h)

outside the Ni/(Ca@Si) nanoreactors. As a comparison, the surface of (Ni/Ca)@Si is cleaner, which might contribute to the stable shell in cycles. It is reasonable to infer that the well-designed shell construction is an effective strategy to defer the CaO sintering and hence promote the CO_2 capture stabilities. Notably, the carbon deposition would harm the following CO_2 capture step by diluting the toxic CO in the exhaust gas from a process point of view. Introducing an extra intermediate step, e. g., steam purge[55], might be applicable to eliminate the CO emission and by-producing syn gas in the deployment of ICCU-DRM.

$$CH_4 = C + 2H_2 \tag{9}$$

The metal particle size of Ni was believed to be sensitive in CH_4 decomposition (Eq.9) and carbon nanotube growth[56,57]. Larger Ni clusters are more prone to generate carbon deposition in DRM[58]. Hence, even though the Ni on Ni/(Ca@Si) might be more easily exposed in CH_4, it still exhibits less carbon deposition due to the best dispersion. As summarized in Figure S3, Ni/Ca exhibited the largest initial particle sizes (∼ 13.31 nm) and performed the highest CO yield in the CO_2 capture step in the 2nd ICCU cycle (Fig. 6b). With the decreasing of Ni sizes from 12.12 nm on (Ni/Ca)@Si to 9.96 nm on Ni/(Ca@Si), the CO yield in the CO_2 capture step (twice the amount of carbon deposits) reduced from 6.61 to 2.49 mmol/g. Interestingly, the carbon deposit amounts decrease with cycles, while the statistical metal particle sizes increase to varying degrees. The H_2:CO exhibited a similar decreasing trend, representing the CH_4 decomposition was gradually hindered in cycles. Notably, the Ni/Ca exhibits a stable H_2:CO ratio but a decreased
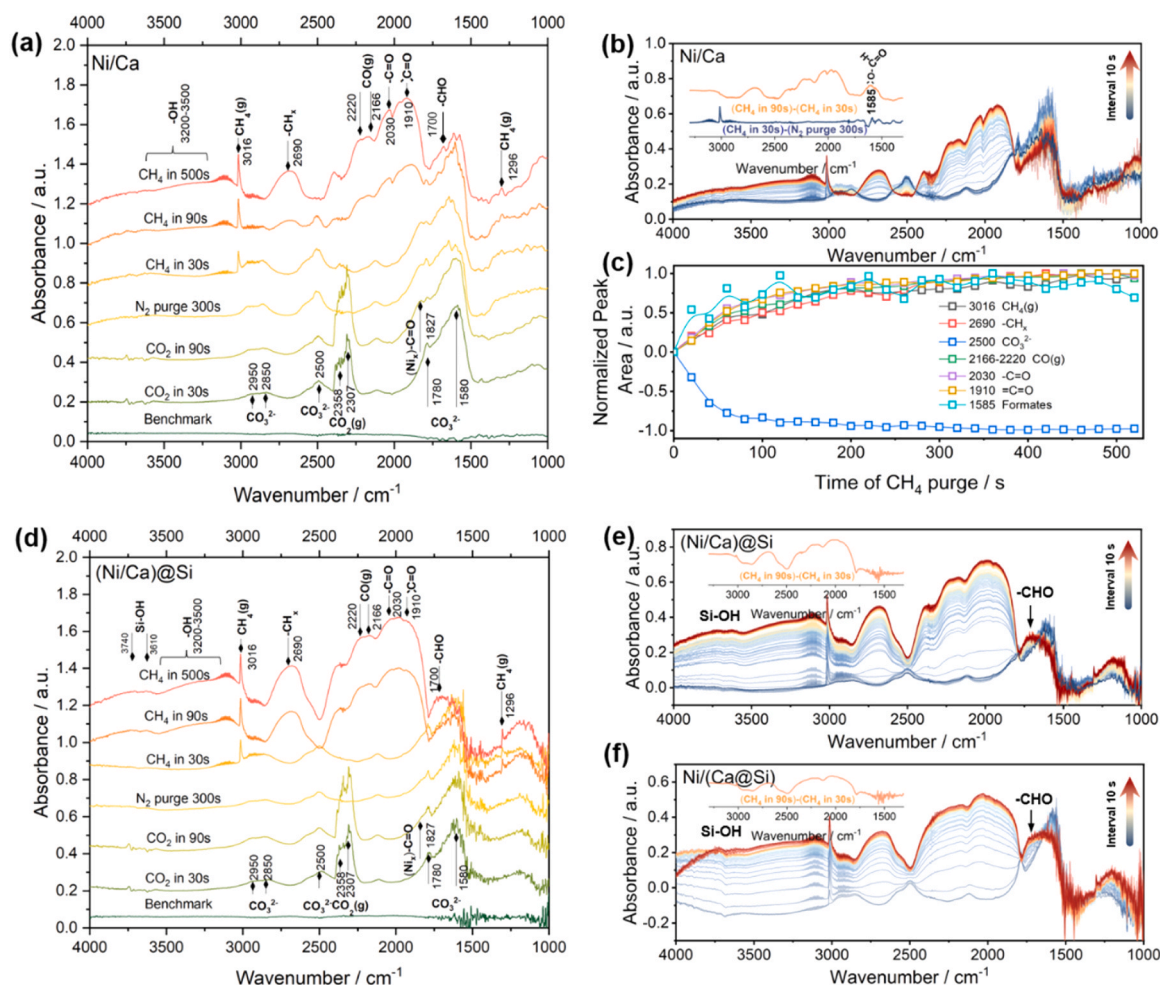

Fig. 9. Isothermal in situ DRIFTS of Ni/Ca material: detailed stacked spectra of ICCU-DRM (a); merged spectra of the integrated DRM step (b); evolvement of normalized selected peak area with time curves (c). Isothermal in situ DRIFTS of (Ni/Ca)@Si and Ni/(Ca@Si) nanoreactors: detailed stacked spectra of ICCU-DRM using (Ni/Ca)@Si nanoreactor (d); merged spectra of the integrated DRM step using (Ni/Ca)@Si (e) and Ni/(Ca@Si) (f) nanoreactors.
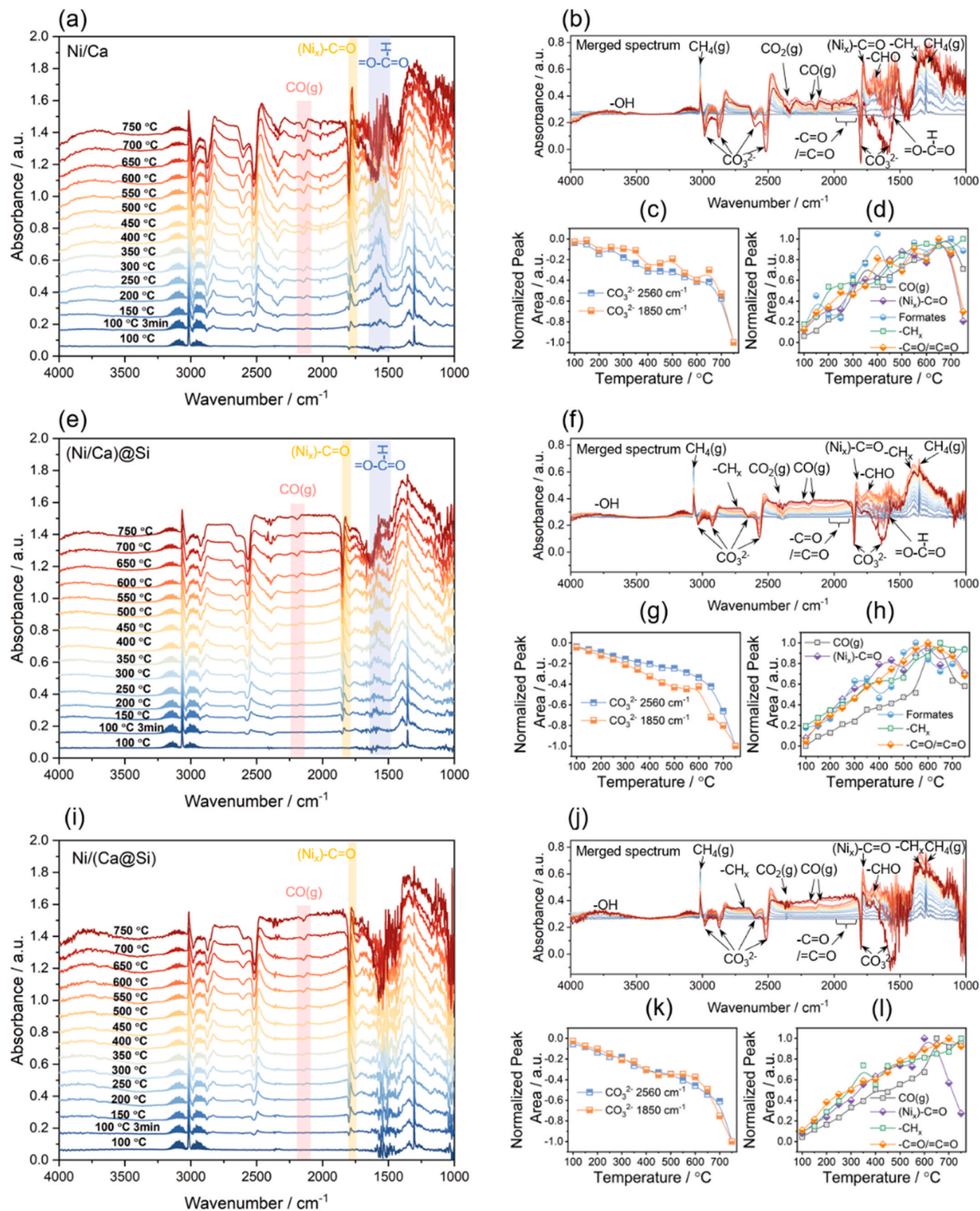
Fig. 10. Stacked and merged DRIFTS spectra of temperature-programmed DRM of (a and b) Ni/Ca, (e and f) (Ni/Ca)@Si and (i and j) Ni/(Ca@Si) nanoreactors. Evolvement of normalized selected peak area with temperature curves of (c and d) Ni/Ca, (g and h) (Ni/Ca)@Si and (k and l) Ni/(Ca@Si) nanoreactors.

carbon deposition amount, which is mainly attributed to the decreased DRM time consumption due to the declined CO2 capacities in cycles. It was reported that the CaO went through intense dynamic volume change in cyclic carbonation-decomposition[59], which induces the formation of encapsulated Ni. Furthermore, the Ca_2SiO_4 shell also dynamically changes, as evidenced by Fig. 7. In summary, the encapsulation of Ni by Ca_2SiO_4 and CaO is responsible for the gradually decreasing amount of carbon deposition and H_2:CO ratio.

The CO_2 conversion is the most pivotal indicator to evaluate the catalytic performance in the integrated DRM process. It is noted that the (Ni/Ca)@Si nanoreactor outperforms the other two counterparts, as detailed in Fig. 6c. Such results successfully demonstrated the effectiveness of the confined catalysis strategy. For Ni/Ca material, the CO_2 generated from carbonate decomposition most likely misses nearby catalytic sites. For Ni/(Ca@Si), although the decomposed CO_2 was well confined by the Ca_2SiO_4 shell, the residual CO_2 in the cavities had no chance to contact catalysts. Constructing active sites inside the shell would convert the confined CO_2 more thoroughly and hence exhibit enhanced catalytic performance. On the other hand, all three candidates exhibited impressive stabilities with no distinct CO_2 conversion rate decrease. However, as cyclic real-time results shown in Figure S4, the (Ni/Ca)@Si and Ni/(Ca@Si) perform a decrease in instantaneous CO yield, which is highly attributed to the hinderance of the Ca_2SiO_4 shell. It is suggested that the shell structure (e.g. thickness, porosity) should be carefully designed to achieve confined catalysis and satisfactory kinetics.

Consistent with the stable catalytic performance, there is no distinct change in the phase composition (Fig. 8a). Furthermore, the Ca_2SiO_4 phase on Ni/(Ca@Si) exhibits higher crystallinity compared to (Ni/Ca) @Si, as illustrated in the inserted patterns in Fig. 8a. The crystallinity of the Ca_2SiO_4 shell could be clearly evidenced by TEM images in Fig. 7, in which the (Ni/Ca)@Si performs much thinner crystals.

Furthermore, the CaO yolks and Ca_2SiO_4 shells went through dynamic changes in cycles of ICCU, which could be further evidenced by porosity in Fig. 8b. In general, the (Ni/Ca)@Si and Ni/(Ca@Si) nanoreactors perform higher surface areas (Table S2) and more abundant micro/mesopores, which are attributed to the yolk-shell structure. Compared to the as-synthesized materials (Fig. 2d), all the NiSiCa-based materials show better mesopores, even distinctly sintered (e.g. Ni/Ca, Fig. 7a). In previous studies, it was found that the dynamic volume change of CaO-based materials in carbonation/decomposition would induce abundant cracks during sintering[19,60]. Here, we suggest that the sintering of CaO does not always exhibit pore structure loss and a decrease in specific surface area.

The Raman spectrum could characterize the detailed information of carbon species with different orderliness. As illustrated in Fig. 8c, the D band at ∼ 1357 cm^{-1} and G band at 1579 cm^{-1} identify the amorphous/ disordered carbon and sp^2 stretching vibration of graphitic carbon species, respectively[61,62]. The intensity ratio of D and G bands was therefore widely applied to characterize the degree of graphitization[63, 64]. As exhibited in Fig. 8c, the Ni/Ca performs the lowest I_D:I_G ratio (0.76) and highest carbon deposition amount (Fig. 6b), indicating the growth of large amounts of graphitized carbon or nanotubes (also evidenced by Fig. 7a). The (Ni/Ca)@Si and Ni/(Ca@Si) nanoreactors are more intent to induce amorphous carbon, of which the Ni/(Ca@Si) exhibits the highest I_D:I_G ratio (1.20). By jointly analyzing the carbon deposit amounts of all three materials (Fig. 8b), it is clear that the formation of amorphous carbon is negatively correlated to the generation of carbon nanotubes. It has been proven an effective strategy by impeding the migration of carbon species on the metal clusters' surface to inhibit the growth of carbon nanotubes[65]. In line with the abovementioned discussion, the encapsulation extent of Ni is negatively corrected to the carbon deposit amount. The carbon deposition would be gasified into toxic CO in the CO_2 capture step and harm the exhaust gas. Therefore, the best scenario in the integrated DRM step is to selectively catalyze DRM with no CH_4 decomposition. The constructed

nanoreactors deliver such expectations brilliantly with even enhanced catalytic activities (Fig. 6c).

3.4. In situ diffused reflectance infrared fourier transform spectroscopy (DRIFTS)

The reaction mechanism and potential intermediates were studied with in situ DRIFTS under isothermal conditions (650 °C), as shown in Fig. 9. The CO_2 capture step of all the NiSiCa-based materials performs similar species changes. As detailed in Figs. 9a and d, a group of peaks belonging to carbonates emerged and quickly saturated (i.e. 30 s) on the surface during CO_2 capture, including ∼ 2950, 2850, 2500, 1780 and 1580 cm^{-1}[19]. The surface reaction of CaO and CO_2 is reported as a chemical reaction-controlled process with fast kinetics[66], explaining the rapid saturation of surface carbonates. To supplement carbonates in the bulk phase for the following DRM, we performed the carbonation step for 90 seconds. Interestingly, as shown in Fig. 9a, a peak at ∼ 1827 cm^{-1} gradually emerged on Ni/Ca after 90 s' CO_2 capture, which is contributed by the formation of multidentate carbonyls (Nix-C≡O) [67]. However, the counterpart nanoreactors (Fig. 9d and S6) did not generate such species under the same CO_2 exposure conditions. It was reported that the Ni would decompose CO_2 and be oxidized via carbonyl intermediates[68,69]. The Ni clusters on Ni/Ca are larger and, hence, might be more prone to yield stable multidentate carbonyl species.

The surface carbonates species showed no distinct change after ∼ 300 s N_2 purge, nor did stable bridging carbonyl species. Subsequently, the CH_4 was introduced to investigate the integrated DRM process. As shown in Fig. 9a, the peaks at 3016 and 1296 cm^{-1} are attributed to the C-H stretching and bending vibrations of CH_4, respectively[70]. The integrated DRM is slower compared to surface carbonation in in situ DRIFTS. As evidenced in the inserted patterns in Fig. 9b, no apparent new species formed on the subtracted spectrum after 30 s' CH_4 exposure. Subsequently, several key intermediates emerged with time on Ni/Ca accompanied by surface carbonates consumption (Fig. 9a, b and c). Notably, the consuming carbonates species (∼1580 cm^{-1}) and generating formates (∼ 1585 cm^{-1})[70,71] are highly overlapped, and the emerged formates could be identified by deducting the previous spectrum (the insert pattern in Fig. 9b). Moreover, the carbon, formed from CH_4 decomposition, might be oxidized by surface hydroxyl to form -CHO species (∼ 1700 cm^{-1})[72]. Specifically, CHx (2690 cm^{-1}), linearly coordinated carbonyls (-C≡O, 2030 cm^{-1}), bridging carbonyls (=C≡O, 1910 cm^{-1})[73], -CHO (1700 cm^{-1}), formates (HCOO, 1585 cm^{-1}) and gaseous CO (2220 and 2166 cm^{-1}) gradually increased and reached the maximum level at ∼ 200 s. Subsequently, the bulk carbonates replenish CO_2 to the surface for DRM. Due to the sensitivity of surface characterization, it is difficult to observe the complete disappearance of key species within a limited time (i.e., 500 s). Similar to Ni/Ca, the (Ni/Ca)@Si and Ni/(Ca@Si) nanoreactors exhibit the increasing of carbonyls and CHO species while yielding gaseous CO (Fig. 9d and S6). Differently, the formates species are invisible, which might be masked by the consumption of carbonates (∼ 1580 cm^{-1}). It at least proves that the formates formation on nanoreactors is not as significant as Ni/Ca. Furthermore, the (Ni/Ca)@Si (Fig. 9e) and Ni/(Ca@Si) (Fig. 9f) show more distinct CHO groups compared to Ni/Ca (Fig. 9b), which are attributed to the abundant Si-OH groups (∼ 3700 cm^{-1})[74].

The in situ DRIFTS was also conducted at various temperatures to identify the temperature sensitivity of the formation of intermediates. Before temperature-programmed DRIFTS evaluation, the materials were thoroughly carbonated at 650 °C for 30 min. As shown in Fig. 10a and b, the intermediates, including carbonyls, formates and CHO species, could form on Ni/Ca at low temperatures (e.g., 100 °C). The gaseous CO could be generated at ∼ 200 °C but with low kinetics. With the temperature increase, the surface carbonates were gradually consumed. The consumption rate of carbonates significantly increases from ∼ 650 °C (Fig. 10c, g and k), accompanied by the maximum intermediates peak
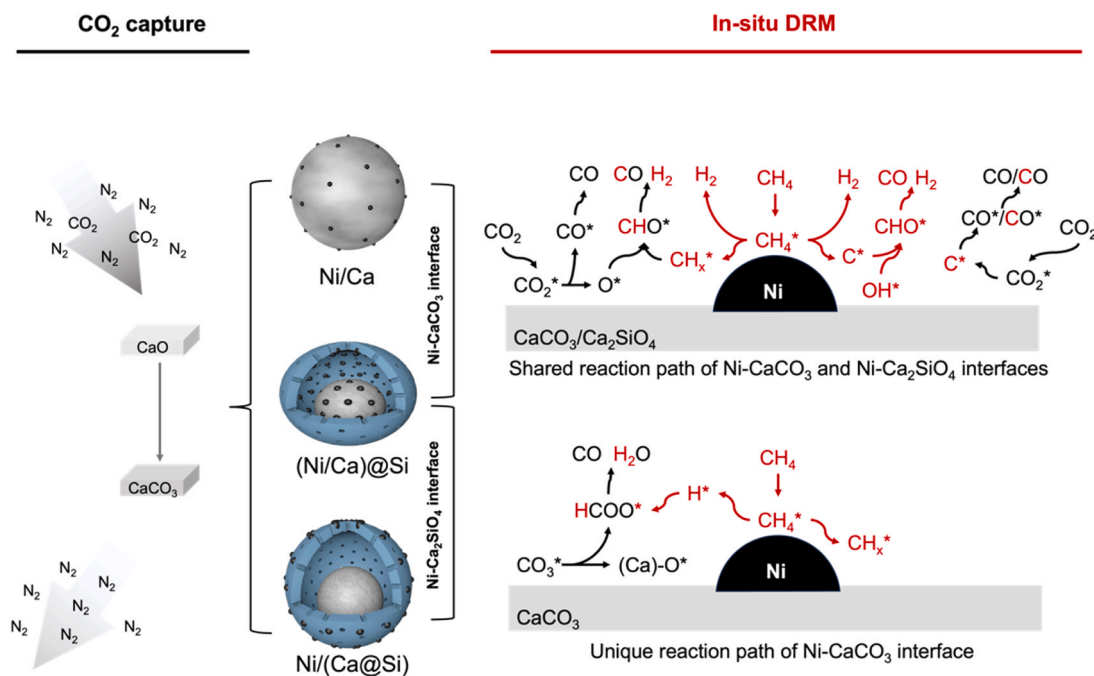
Fig. 11. Mechanism diagram of ICCU-DRM over Ni/Ca, (Ni/Ca)@Si and Ni/(Ca@Si) nanoreactors.

area and CO yields (Fig. 10d, h and i). Importantly, the temperature-programmed DRIFTS identified the various intermediate species on the three candidates. Specifically, carbonyls, formates and CHO species were characterized on Ni/Ca and (Ni/Ca)@Si, while no formates species were detected on Ni/(Ca@Si).

As demonstrated in Fig. 11, the universal mechanism of CO_2 capture is the formation of $CaCO_3$. Subsequently, the CH_4 decomposes into CH_x/ C and H on Ni and releases H_2 by combining two H. The CO_2/CO_3^{2-} could dissociate on Ni surface and yield carbonyl species and then desorbed into gas, simultaneously supplying O for C gasification. The C might also be oxidized by surface OH as an intermediate (CHO) for CO generation. Differently, the Ni/Ca and (Ni/Ca)@Si, with Ni-$CaCO_3$ interfaces, exhibited the formates intermediates, which are absent on Ni/(Ca@Si). The formate intermediate most likely generates from the direct reaction of spillovered hydrogen with carbonates. In summary, the Ni catalyzes the DRM potentially via carbonyls and CHO intermediates, while the formate intermediate is dependent on the Ni-carbonates interface in the integrated DRM.

4. Conclusion

Inspired by confined catalysis, Ni-functionalized Ca@Si yolk-shell nanoreactors were constructed using novel dry-ice precipitation and silane hydrolysis methods. The Ca_2SiO_4 shell hindered the sintering of CaO and tailored the diffusion of decomposed CO_2 in the integrated DRM process. By doping Ni inside the Ca_2SiO_4 shell, the confined CO_2 could thoroughly react with CH_4 and stably exhibit ~ 92% CO_2 conversion in 10 cycles at 650 °C. The local structure of active sites could be critically tuned by doping Ni in/out of the Ca_2SiO_4 shell to evaluate the catalytic roles of Ni-carbonates or Ni-Ca_2SiO_4 interfaces. Based on in situ DRIFTS investigations, it is found that the integrated DRM could be catalyzed via carbonyls, formates and CHO intermediate steps, while the formates are highly related to the Ni-carbonates interface. The reported confined catalysis directed nanoreactor construction and identified potential intermediates provide valuable reference and portable strategy for further deployments on ICCU and other heterogeneous catalytic processes.

CRediT authorship contribution statement

Zhu Yuan: Investigation. **Sun Shuzhuang:** Writing – review & editing, Writing – original draft, Methodology, Investigation, Formal analysis, Data curation, Conceptualization. **Xu Yongqing:** Writing – review & editing, Supervision, Methodology, Investigation, Formal analysis. **Wu Mengna:** Formal analysis. **Zhang Chen:** Investigation. **Wang Yuanyuan:** Methodology, Investigation, Formal analysis. **Zhou Hui:** Writing – review & editing, Supervision, Resources, Funding acquisition. **Xu Yikai:** Methodology, Formal analysis, Conceptualization. **Wu Chunfei:** Writing – review & editing, Supervision, Resources, Project administration, Funding acquisition, Conceptualization. **Sun Hongman:** Writing – review & editing, Investigation. **Yang Xiaoxiao:** Formal analysis. **Bie Xuan:** Investigation, Formal analysis. **Zhao Xiaotong:** Investigation, Formal analysis. **Zhang Yingrui:** Investigation, Formal analysis.

Declaration of Competing Interest

The authors declare that they have no known competing financial interests or personal relationships that could have appeared to influence the work reported in this paper.

Data availability

Data will be made available on request.

Acknowledgments

Appendix A. Supporting information

Supplementary data associated with this article can be found in the

online version at doi:10.1016/j.apcatb.2024.123838.

References

[1] Z. Hao, M.H. Barecka, A.A. Lapkin, Accelerating net zero from the perspective of optimizing a carbon capture and utilization system, Energy Environ. Sci. 15 (2022) 2139–2153.

[2] K. Akimoto, F. Sano, J. Oda, H. Kanaboshi, Y. Nakano, Climate change mitigation measures for global net-zero emissions and the roles of CO_2 capture and utilization and direct air capture, Energy Clim. Change 2 (2021) 100057.

[3] G.T. Rochelle, Amine scrubbing for CO_2 capture, Science 325 (2009) 1652–1654.

[4] F. Meng, Y. Meng, T. Ju, S. Han, L. Lin, J. Jiang, Research progress of aqueous amine solution for CO_2 capture: a review, Renew. Sustain. Energy Rev. 168 (2022) 112902.

[5] M. Erans, V. Manovic, E.J. Anthony, Calcium looping sorbents for CO_2 capture, Appl. Energy 180 (2016) 722–742.

[6] Y. Xu, H. Ding, C. Luo, Y. Zheng, Y. Xu, X. Li, Z. Zhang, C. Shen, L. Zhang, Effect of lignin, cellulose and hemicellulose on calcium looping behavior of CaO-based sorbents derived from extrusion-spherization method, Chem. Eng. J. 334 (2018) 2520–2529.

[7] R. Han, Y. Wang, S. Xing, C. Pang, Y. Hao, C. Song, Q. Liu, Progress in reducing calcination reaction temperature of calcium-looping CO_2 capture technology: a critical review, Chem. Eng. J. 450 (2022) 137952.

[8] B. Jin, R. Wang, D. Fu, T. Ouyang, Y. Fan, H. Zhang, Z. Liang, Chemical looping CO_2 capture and in-situ conversion as a promising platform for green and low-carbon industry transition: review and perspective, Carbon Capture Sci. Technol. (2023) 100169.

[9] C. da Silveira Cachola, M. Ciotta, A.A. dos Santos, D. Peyerl, Deploying of the carbon capture technologies for CO_2 emission mitigation in the industrial sectors, Carbon Capture Sci. Technol. (2023) 100102.

[10] S. Sun, H. Sun, S. Guan, S. Xu, C. Wu, Integrated CO_2 capture and methanation on Ru/CeO₂-MgO combined materials: morphology effect from CeO₂ support, Fuel 317 (2022) 123420.

[11] S. Sun, Y. Zhang, C. Li, Y. Wang, C. Zhang, X. Zhao, H. Sun, C. Wu, Upgrading CO2 from simulated power plant flue gas via integrated CO2 capture and dry reforming of methane using Ni-CaO, Sep. Purif. Technol. 308 (2023).

[12] M. Usman, W. Daud, H.F. Abbas, Dry reforming of methane: influence of process parameters-a review, Renew. Sustain. Energy Rev. 45 (2015) 710–744.

[13] C. Palmer, D.C. Upham, S. Smart, M.J. Gordon, H. Metiu, E.W. McFarland, Dry reforming of methane catalysed by molten metal alloys, Nat. Catal. 3 (2020) 83–89.

[14] W.Y. Hong, A techno-economic review on carbon capture, utilisation and storage systems for achieving a net-zero CO_2 emissions future, Carbon Capture Sci. Technol. 3 (2022) 100044.

[15] M.S. Duyar, M.A.A. Trevino, R.J. Farrauto, Dual function materials for CO_2 capture and conversion using renewable H_2, Appl. Catal. B: Environ. 168 (2015) 370–376.

[16] S. Sun, H. Sun, P.T. Williams, C. Wu, Recent advances in integrated CO_2 capture and utilization: a review, Sustain. Energy Fuels 5 (2021) 4546–4559.

[17] J. Chen, Y. Xu, P. Liao, H. Wang, H. Zhou, Recent progress in integrated CO_2 capture and conversion process using dual function materials: a state-of-the-art review, Carbon Capture Sci. Technol. 4 (2022) 100052.

[18] Z. Lv, S. Chen, X. Huang, C. Qin, Recent progress and perspective on integrated CO_2 capture and utilization, Curr. Opin. Green Sustain. Chem. (2023) 100771.

[19] S. Sun, Z. Lv, Y. Qiao, C. Qin, S. Xu, C. Wu, Integrated CO_2 capture and utilization with CaO-alone for high purity syngas production, Carbon Capture Sci. Technol. 1 (2021) 100001.

[20] H. Sun, J. Wang, J. Zhao, B. Shen, J. Shi, J. Huang, C. Wu, Dual functional catalytic materials of Ni over Ce-modified CaO sorbents for integrated CO_2 capture and conversion, Appl. Catal. B: Environ. 244 (2019) 63–75.

[21] S. Sun, C. Zhang, Y. Wang, X. Zhao, H. Sun, C. Wu, CO_2 capture from H_2O and O_2 containing flue gas integrating with dry reforming methane using Ni-doping CaO dual functional materials, Chem. Eng. J. 468 (2023) 143712.

[22] J. Hu, P. Hongmanorom, Z.Li Galvita, S. Kawi, Bifunctional Ni-Ca based material for integrated CO_2 capture and conversion via calcium-looping dry reforming, Appl. Catal. B: Environ. 284 (2021) 119734.

[23] X. Zhao, S. Sun, Y. Zhang, Y. Wang, Y. Zhu, P. Williams, S. Guan, C. Wu, Synergistic performance of Ni-Ca based dual functional materials under the coexistence of moisture and oxygen in CO_2 source for integrated carbon capture and utilisation, Sep. Purif. Technol. 326 (2023) 124866.

[24] S. Sun, Y. Zhang, C. Li, Y. Wang, C. Zhang, X. Zhao, H. Sun, C. Wu, Upgrading CO_2 from simulated power plant flue gas via integrated CO_2 capture and dry reforming of methane using Ni-CaO, Sep. Purif. Technol. 308 (2023) 122956.

[25] B. Jin, T. Ouyang, Z. Zhang, Y. Zhao, H. Zhang, W. Yao, G. Huang, Z. Liang, Prussian blue derived Ca-Fe bifunctional materials for chemical looping CO_2 capture and in-situ conversion, Sep. Purif. Technol. 320 (2023) 123975.

[26] S. Tian, F. Yan, Z. Zhang, J. Jiang, Calcium-looping reforming of methane realizes in situ CO_2 utilization with improved energy efficiency, Sci. Adv. 5 (2019) eaav5077.

[27] S.M. Kim, P.M. Abdala, M. Broda, D. Hosseini, C. Coperet, C. Muller, Integrated CO_2 capture and conversion as an efficient process for fuels from greenhouse gases, ACS Catal. 8 (2018) 2815–2823.

[28] R.E. Owen, Y.S. Zhang, T.P. Neville, G. Manos, P.R. Shearing, D.J. Brett, J.J. Bailey, Visualising coke-induced degradation of catalysts used for CO_2-reforming of methane with X-ray nano-computed tomography, Carbon Capture Sci. Technol. 5 (2022) 100068.

[29] L. Zhu, Z. Lv, X. Huang, S. Lu, J. Ran, C. Qin, Development of dual-functional materials for integrated CO_2 capture and utilization by dry reforming of CH_4, Fuel Process. Technol. 248 (2023) 107838.

[30] T.A. Shifa, A. Vomiero, Confined catalysis: progress and prospects in energy conversion, Adv. Energy Mater. 9 (2019) 1902307.

[31] M. Sanlés-Sobrido, M. Pérez-Lorenzo, B. Rodríguez-González, V. Salgueiriño, M. A. Correa-Duarte, Highly active nanoreactors: nanomaterial encapsulation based on confined catalysis, Angew. Chem. 124 (2012) 3943–3948.

[32] L. Liu, A. Corma, Confining isolated atoms and clusters in crystalline porous materials for catalysis, Nat. Rev. Mater. 6 (2021) 244–263.

[33] X. Wu, R. Chang, M. Tan, L. Tao, Q. Fan, X. Hu, H.L. Tan, M. Åhlén, O. Cheung, W. Liu, An investigation of the Ni/carbonate interfaces on dual function materials in integrated CO_2 capture and utilisation cycles, Appl. Catal. B: Environ. 338 (2023) 123053.

[34] H. Sun, Y. Wang, S. Xu, A.I. Osman, G. Stenning, J. Han, S. Sun, D. Rooney, P. T. Williams, F. Wang, Understanding the interaction between active sites and sorbents during the integrated carbon capture and utilization process, Fuel 286 (2021) 119308.

[35] F. Donnelly, F. Purcell-Milton, V. Framont, O. Cleary, P. Dunne, Y. Gun'ko, Synthesis of $CaCO_3$ nano-and micro-particles by dry ice carbonation, Chem. Commun. 53 (2017) 6657–6660.

[36] T. Ogino, T. Suzuki, K. Sawada, The formation and transformation mechanism of calcium carbonate in water, Geochim. Et. Cosmochim. Acta 51 (1987) 2757–2767.

[37] Y.S. Han, G. Hadiko, M. Fuji, M. Takahashi, Effect of flow rate and CO_2 content on the phase and morphology of $CaCO_3$ prepared by bubbling method, J. Cryst. Growth 276 (2005) 541–548.

[38] B. Feng, A.K. Yong, H. An, Effect of various factors on the particle size of calcium carbonate formed in a precipitation process, Mater. Sci. Eng.: A 445 (2007) 170–179.

[39] S. El-Sheikh, S. El-Sherbiny, A. Barhoum, Y. Deng, Effects of cationic surfactant during the precipitation of calcium carbonate nano-particles on their size, morphology, and other characteristics, Colloids Surf. A: Physicochem. Eng. Asp. 422 (2013) 44–49.

[40] M. Khoeini, A. Najafi, H. Rastegar, M. Amani, Improvement of hollow mesoporous silica nanoparticles synthesis by hard-templating method via CTAB surfactant, Ceram. Int. 45 (2019) 12700–12707.

[41] A.A. Scaltsoyiannes, A.A. Lemonidou, On the factors affecting the deactivation of limestone under calcium looping conditions: a new comprehensive model, Chem. Eng. Sci. 243 (2021) 116797.

[42] S. Tougaard, Quantitative XPS: non-destructive analysis of surface nano-structures, Appl. Surf. Sci. 100 (1996) 1–10.

[43] J. Cañón, A.V. Teplyakov, XPS characterization of cobalt impregnated SiO_2 and γ-Al_2O_3, Surf. Interface Anal. 53 (2021) 475–481.

[44] A.J. Majewski, J. Wood, W. Bujalski, Nickel–silica core@ shell catalyst for methane reforming, Int. J. Hydrog. Energy 38 (2013) 14531–14541.

[45] M. Kaviani, M. Rezaei, S.M. Alavi, E. Akbari, High coke resistance Ni-SiO_2@ SiO_2 core-shell catalyst for biogas dry reforming: effects of Ni loading and calcination temperature, Fuel 330 (2022) 125609.

[46] M. Kosari, S. Askari, A.M. Seayad, S. Xi, S. Kawi, A. Borgna, H.C. Zeng, Strong coke-resistivity of spherical hollow Ni/SiO_2 catalysts with shell-confined high-content Ni nanoparticles for methane dry reforming with CO_2, Appl. Catal. B: Environ. 310 (2022) 121360.

[47] X. Xie, D. Liang, D. Chen, Y. Wang, W. Li, J. Wang, L. Yuan, Dry reforming of methane over silica zeolite-encapsulated Ni-based catalysts: Effect of preparation method, support structure and Ni content on catalytic performance, Int. J. Hydrog. Energy 48 (2023) 7319–7336.

[48] T. Pu, J. Chen, W. Tu, J. Xu, Y.-F. Han, I.E. Wachs, M. Zhu, Dependency of CO_2 methanation on the strong metal-support interaction for supported Ni/CeO_2 catalysts, J. Catal. 413 (2022) 821–828.

[49] S. Xu, T.J. Slater, H. Huang, Y. Zhou, Y. Jiao, C.M. Parlett, S. Guan, S. Chansai, S. Xu, X. Wang, Developing silicalite-1 encapsulated Ni nanoparticles as sintering-/coking-resistant catalysts for dry reforming of methane, Chem. Eng. J. 446 (2022) 137439.

[50] P. Burattin, M. Che, C. Louis, Metal particle size in Ni/SiO_2 materials prepared by deposition− precipitation: influence of the nature of the Ni (II) phase and of its interaction with the support, J. Phys. Chem. B 103 (1999) 6171–6178.

[51] W. Liang, H. Yan, C. Chen, D. Lin, K. Tan, X. Feng, Y. Liu, X. Chen, C. Yang, H. Shan, Revealing the effect of nickel particle size on carbon formation type in the methane decomposition reaction, Catalysts 10 (2020) 890.

[52] Y. Xu, C. Luo, H. Sang, B. Lu, F. Wu, X. Li, L. Zhang, Structure and surface insight into a temperature-sensitive CaO-based CO_2 sorbent, Chem. Eng. J. 435 (2022) 134960.

[53] S. Sun, C. Zhang, S. Guan, S. Xu, P.T. Williams, C. Wu, Ni/support-CaO bifunctional combined materials for integrated CO_2 capture and reverse water-gas shift reaction: influence of different supports, Sep. Purif. Technol. 298 (2022) 121604.

[54] L. Fedunik-Hofman, A. Bayon, S.W. Donne, Comparative kinetic analysis of $CaCO_3$/ CaO reaction system for energy storage and carbon capture, Appl. Sci. 9 (2019) 4601.

[55] S. Sun, C. Zhang, Y. Wang, X. Zhao, H. Sun, C. Wu, CO2 capture from H2O and O2 containing flue gas integrating with dry reforming methane using Ni-doping CaO dual functional materials, Chem. Eng. J. 468 (2023).

[56] C.M. Damaskinos, J. Zavašnik, P. Djinović, A.M. Efstathiou, Dry reforming of methane over Ni/$Ce_{0.8}Ti_{0.2}O_{2-\delta}$: the effect of Ni particle size on the carbon pathways studied by transient and isotopic techniques, Appl. Catal. B: Environ. 296 (2021) 120321.

[57] J.W. Han, J.S. Park, M.S. Choi, H. Lee, Uncoupling the size and support effects of Ni catalysts for dry reforming of methane, Appl. Catal. B: Environ. 203 (2017) 625–632.

[58] J.W. Han, C. Kim, J.S. Park, H. Lee, Highly coke-resistant Ni nanoparticle catalysts with minimal sintering in dry reforming of methane, ChemSusChem 7 (2014) 451–456.

[59] J. Chen, L. Duan, Y. Ma, Y. Jiang, A. Huang, H. Zhu, H. Jiao, M. Li, Y. Hu, H. Zhou, Recent progress in calcium looping integrated with chemical looping combustion (CaL-CLC) using bifunctional CaO/CuO composites for CO_2 capture: a state-of-the-art review, Fuel 334 (2023) 126630.

[60] S. Sun, S. He, C. Wu, Ni promoted Fe-CaO dual functional materials for calcium chemical dual looping, Chem. Eng. J. 441 (2022) 135752.

[61] M.S. Dresselhaus, G. Dresselhaus, R. Saito, A. Jorio, Raman spectroscopy of carbon nanotubes, Phys. Rep. 409 (2005) 47–99.

[62] R. Saito, A. Grüneis, G.G. Samsonidze, V. Brar, G. Dresselhaus, M. Dresselhaus, A. Jorio, L. Cançado, C. Fantini, M. Pimenta, Double resonance Raman spectroscopy of single-wall carbon nanotubes, N. J. Phys. 5 (2003) 157.

[63] S. He, Y. Xu, Y. Zhang, S. Bell, C. Wu, Waste plastics recycling for producing high-value carbon nanotubes: Investigation of the influence of manganese content in Fe-based catalysts, J. Hazard. Mater. 402 (2021) 123726.

[64] N. Cai, X. Li, S. Xia, L. Sun, J. Hu, P. Bartocci, F. Fantozzi, P.T. Williams, H. Yang, H. Chen, Pyrolysis-catalysis of different waste plastics over Fe/Al_2O_3 catalyst: high-value hydrogen, liquid fuels, carbon nanotubes and possible reaction mechanisms, Energy Convers. Manag. 229 (2021) 113794.

[65] Z. Bian, I.Y. Suryawinata, S. Kawi, Highly carbon resistant multicore-shell catalyst derived from Ni-Mg phyllosilicate nanotubes@ silica for dry reforming of methane, Appl. Catal. B: Environ. 195 (2016) 1–8.

[66] Z.-s Li, F. Fang, X.-y Tang, N.-s Cai, Effect of temperature on the carbonation reaction of CaO with CO_2, Energy Fuels 26 (2012) 2473–2482.

[67] L. Bobadilla, V. Garcilaso, M. Centeno, J. Odriozola, CO_2 reforming of methane over Ni-Ru supported catalysts: on the nature of active sites by operando DRIFTS study, J. CO_2 Util. 24 (2018) 509–515.

[68] V. De Coster, N.V. Srinath, P. Yazdani, H. Poelman, V.V. Galvita, Does CO_2 oxidize Ni catalysts? A quick X-ray absorption spectroscopy answer, J. Phys. Chem. Lett. 13 (2022) 7947–7952.

[69] Y. Yu, Z. Bian, Z. Wang, J. Wang, W. Tan, Q. Zhong, S. Kawi, CO_2 methanation on $Ni-Ce_{0.8}M_{0.2}O_2$ (M= Zr, Sn or Ti) catalyst: suppression of CO via formation of bridging carbonyls on nickel, Catal. Today (2020).

[70] Y. Wang, L. Yao, Y. Wang, S. Wang, Q. Zhao, D. Mao, C. Hu, Low-temperature catalytic CO_2 dry reforming of methane on $Ni-Si/ZrO_2$ catalyst, ACS Catal. 8 (2018) 6495–6506.

[71] O. Demoulin, M. Navez, P. Ruiz, Investigation of the behaviour of a $Pd/\gamma-Al_2O_3$ catalyst during methane combustion reaction using in situ DRIFT spectroscopy, Appl. Catal. A: Gen. 295 (2005) 59–70.

[72] P. Menon, J. De Deken, G. Froment, Formaldehyde as an intermediate in the steam reforming of methane, J. Catal. 95 (1985) 313–316.

[73] M. Németh, Z. Schay, D. Srankó, J. Károlyi, G. Sáfrán, I. Sajó, A. Horváth, Impregnated Ni/ZrO_2 and Pt/ZrO_2 catalysts in dry reforming of methane: Activity tests in excess methane and mechanistic studies with labeled $^{13}CO_2$, Appl. Catal. A: Gen. 504 (2015) 608–620.

[74] N.J. Abreu, H. Valdés, C.A. Zaror, F. Azzolina-Jury, M.F. Meléndrez, Ethylene adsorption onto natural and transition metal modified Chilean zeolite: an operando DRIFTS approach, Microporous Mesoporous Mater. 274 (2019) 138–148.

[75] B. Shao, Z.-Q. Wang, X.-Q. Gong, H. Liu, F. Qian, P. Hu, J. Hu, Synergistic promotions between CO_2 capture and in-situ conversion on Ni-CaO composite catalyst, Nature Communications 14 (2023) 996.